

Selective Electrocatalytic CO₂ Reduction to CO by an NHC-Based Organometallic Heme Analogue

Allyssa A. Massie, Claudia Schremmer, Isabelle Rüter, Sebastian Dechert, Inke Siewert,* and Franc Meyer*

University of Göttingen, Institute of Inorganic Chemistry, D-37077 Göttingen, Germany

KEYWORDS: electrocatalysis, CO₂ reduction, iron complexes, NHC ligands, macrocyclic ligands, heme analogues, spectro-electrochemistry

ABSTRACT: Molecular first-row transition metal complexes for electrocatalytic CO₂ reduction mostly feature N-donor supporting ligands, iron porphyrins being among the most prominent catalysts. Introducing N-heterocyclic carbene (NHC) ligation has previously shown promising effects for some systems, yet the application of NHC iron complexes for electrochemical CO₂ reduction has so far remained unreported. Herein we show that the macrocyclic tetracarbene iron complex [LFe(NCMe)₂](OTf)₂ (**1**), which can be described as an organometallic heme analogue, mediates selective electrocatalytic CO₂-to-CO conversion with a faradaic efficiency of over 90% and a very high initial observed catalytic rate constant (k_{obs}) of 7,800 s⁻¹. Replacement of an axial MeCN ligand by CO significantly increases the catalyst stability and turnover number, while the rate of catalysis decreases only slightly (k_{obs} = 3,100 s⁻¹). Ferrous complexes with one or two axial CO ligands, [LFe(NCMe)(CO)](OTf)₂ (**1-CO**) and [LFe(CO)₂](OTf)₂ (**1-(CO)₂**), have been isolated and fully characterized. Based on linear sweep voltammogram (LSV) spectroelectro-IR (SEC-IR) studies for **1** and **1-CO**, both under N₂ and CO₂ atmosphere, a mechanistic scenario in anhydrous acetonitrile is proposed. It involves two molecules of CO₂ and results in CO and CO₃²⁻ formation, whereby the first CO₂ binds to the doubly reduced, pentacoordinated [LFe⁰(CO)] species. This work commences the exploration of the reductive chemistry by the widely tunable macrocyclic tetracarbene iron motif, which is topologically similar to hemes but electronically distinct as the strongly σ -donating and redox inactive NHC scaffold leads to metal-centered reduction and population of the exposed d_{z²} orbital, in contrast to ligand-based orbitals in the analogous porphyrin systems.

INTRODUCTION

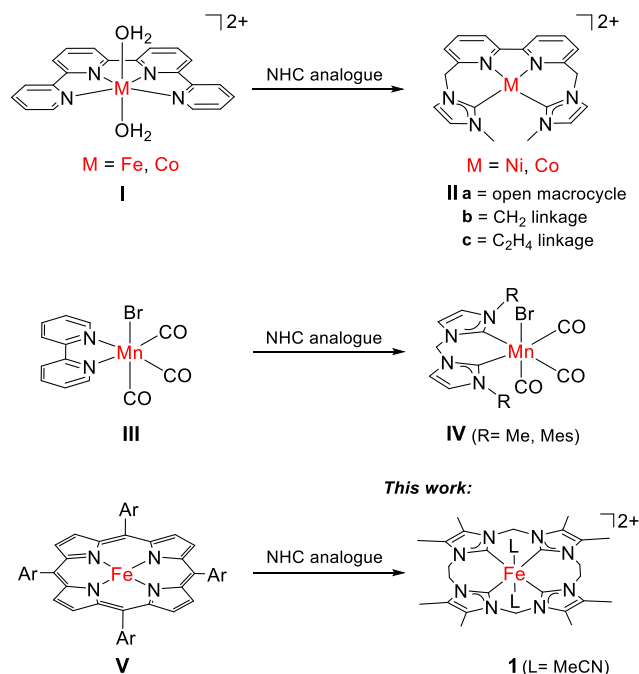
The excess atmospheric CO₂ originating from the unsustainable consumption of fossil fuels is a major cause of global climate change.^{1,2} For good reason, the possibility of using CO₂ to produce electrofuels or C1 building blocks for chemical industry is attracting great interest.^{1,3} While the CO₂ reduction abilities of a wide range of heterogeneous catalysts have shown very promising results, an important benefit of investigating molecular catalysts is the well-defined active site where one can directly investigate correlations between geometric/electronic structures and reactivity. The use of earth abundant metal catalysts for this purpose is particularly attractive and features mainly manganese, iron, cobalt, and nickel.

Electrocatalytic reduction of CO₂ by molecular first-row transition metal catalysts has been most thoroughly studied for Fe-porphyrin (heme-type) systems,^{4,5} and in elegant elaborations the porphyrin ligands have been equipped with pendant proton-relays, mostly using phenol as a proton source.⁴⁻⁸ Attaching trimethylanilinium groups as proton relays allowed Savéant and coworkers to achieve a selective (nearly 100 %) conversion of CO₂ to CO with an impressive turnover frequency of over 10⁶ s⁻¹,⁶ and other second coordination sphere modifications at the porphyrin have led to improvements such as, e.g., reduced O₂ sensitivity or significantly lowered overpotentials.^{6,9-12} Selective CO₂ to CO

electroreduction has also been achieved with non-macrocyclic iron and cobalt complexes based on tetradentate quaterpyridine (qpy) ligands (**I**, Scheme 1).¹³ Both complexes operate at very low overpotential, again with the requirement of a weakly acidic proton source; the Co complex displays TOF values similar to that of iron porphyrins.^{13,14} Another prominent class of 3d metal based CO₂ reduction catalysts, inspired by classical rhenium-based systems, is the MnBr(bpy)(CO)₃ type series of complexes, first introduced by the Deronzier group (**III**, Scheme 1, bpy = 2,2'-bipyridine).¹⁵ Such Mn catalysts were later equipped with bulky substituents to prevent Mn-Mn dimerization,¹⁶ and this tunable platform has been widely modified to provide a deeper mechanistic understanding of CO₂ reduction catalysis.¹⁷⁻²¹

The complexes mentioned so far, as well as most other reported first-row transition metal electrocatalysts for the reduction of CO₂, feature supporting N-donor ligands.²² Recent work has started to address the effects of alternative ligation, in particular that of N-heterocyclic carbenes (NHCs), on the efficiency and stability of CO₂ reduction catalysts.²³⁻²⁵ One successful approach retains the overall structural motif of the established 3d metal catalyst systems but replaces one or more N-donor units by NHCs. Jurss and coworkers reported a series of nickel^{26,27} and cobalt²⁸ electrocatalysts whose tetradentate macrocyclic and nonmacrocyclic bpy-NHC hybrid ligands (**II**, Scheme 1) bear close

similarities with the qpy scaffold (**1**, Scheme 1); a comparison between the Co-qpy and the best bpy-NHC complex, where the two NHC units were linked to give a macrocycle, showed selectivities and Faradaic efficiencies that are quite similar.^{13, 14, 28} Systematic effects of both ligand perturbation and the influences of the metal atom described in these studies highlight the fine tuning necessary to produce good electrocatalysts for CO₂ reduction. An organometallic analogue of the prominent manganese *fac*-tricarbonyl platform **III** has been obtained by replacing the potentially redox active bpy ligand with a bidentate bis(NHC) ligand (**IV**, Scheme 1).²⁹ This organometallic catalyst has been further modified with sterically bulky substituents on the peripheral N groups of the NHC ligands to avoid any potential dimerization. In fact, both Mn-NHC catalysts **IV** show turnover frequencies (TOFs) that exceed those of the parent Mn-bpy catalyst **III**, presumably due to the more electron donating properties of the ligand.^{16, 21, 29, 30} These studies lead one to consider a purely organometallic analogue **1** of the classical Fe-porphyrin **V** as a promising electrocatalyst for CO₂ reduction (Scheme 1). Iron complexes supported by macrocyclic tetracarbene ligand scaffolds have been intensively studied in recent years, but the focus has been on their use in oxidation/oxygenation³¹⁻³⁶ and aziridination chemistry³⁷⁻³⁹ as well as the isolation of high-valent and biorelevant reactive intermediates.⁴⁰⁻⁴⁴ In contrast, the reductive chemistry of such "organometallic heme analogues"^{35, 45} has hardly been studied so far.



Scheme 1. Related N-donor and NHC-ligated electrocatalysts for the reduction of CO₂; **1** is studied in this work.

Here we report on the use of the Fe-tetracarbene complex **1** (Scheme 1) as a precatalyst for the selective electrochemical CO₂-to-CO conversion. Key considerations that motivate the choice of these organometallic heme analogues are: (i) the macrocyclic tetracarbene ligand scaffold is topologically similar to a porphyrin, but is expected to be redox inactive, thus confining all redox chemistry to the central metal ion;

and (ii) the equatorial ligation with four very strong σ -donor NHCs pushes the $d_{x^2-y^2}$ orbital high in energy,⁴⁰ so that reduction of the Fe^{II}(d⁶) complex **1** will necessarily populate its d_{z^2} orbital. Low-valent formal Fe⁰ species are usually implicated as the reactive species in Fe-porphyrin mediated CO₂ electroreduction,^{46, 47} but computational and spectroscopic studies revealed that the reduction is ligand-centered and that they are best described as having an intermediate-spin Fe^{II} center that is antiferromagnetically coupled to a porphyrin diradical anion.^{48, 49} In contrast, an analogous Fe⁰ species derived from tetra(NHC) based **1** may be expected to feature a $(d_{z^2})^2$ configuration, potentially exhibiting super-nucleophilic behavior like that seen in reduced cobalamins.⁵⁰ As an additional benefit, the macrocyclic tetra(NHC) ligand platform offers a wide range of tunability including modification of the ring-size or the peripheral substituents at the NHC subunits.⁵¹⁻⁵³

RESULTS AND DISCUSSION

Complex **1** has been synthesized as previously reported.⁵¹ The inset of Figure 1 (black and blue) shows the redox chemistry of **1** under a N₂ atmosphere in MeCN. **1** exhibits a reduction process at a peak potential E_{pa} of -2.11 V and a reverse feature at E_{pa} = -1.98 V ($v = 0.1 \text{ V s}^{-1}$, Figure S1-S3, all potentials in this paper are referenced *versus* the Fc^{+/0} redox couple). The shape of the anodic and cathodic peak is characteristic for an equilibrium reaction preceding the reversible electron transfer, presumably acetonitrile dissociation.⁵⁴ A second irreversible reduction process appears at a peak potential E_{pc} of -2.55 V followed a shoulder at a peak potential E_{pc} of -2.7 V. In the reverse scan, two additional oxidation events can be seen at $E_{pa,2}$ of -1.08 and $E_{pa,3}$ of -0.77 V when the potential has been scanned reductively beyond -2.5 V (Figure 1, inset).

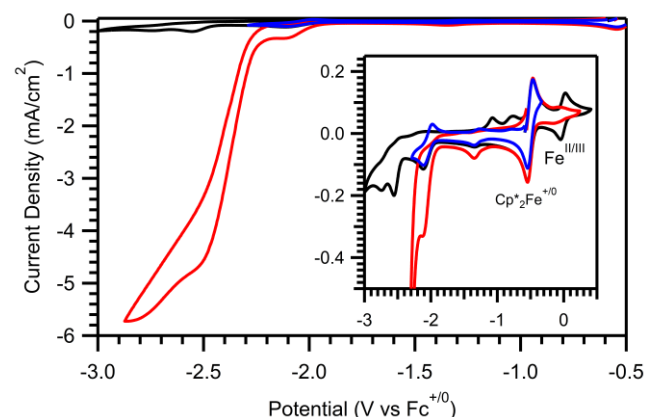


Figure 1. CV of 0.5 mM **1** under a N₂ (black, blue) or CO₂ (red) atmosphere in MeCN + 0.1 M Bu₄NPF₆ at 0.1 V/s with a glassy carbon working electrode. Inset shows reduction under N₂ atmosphere (black, blue) as well as pre-wave of CO₂ reduction wave (red).

Under a CO₂ atmosphere, the CV data of **1** show the appearance of a large current increase with a half peak potential⁵⁵ of -2.35 V for the catalytic wave, which indicates CO₂ reduction catalyzed by **1** (Figure 1). The wave exhibits a pre-wave that occurs at nearly the same potential as the first reduction process of **1** under a N₂ atmosphere (Figure 1, inset). In

order to confirm CO₂-reduction catalysis, controlled potential electrolysis experiments (CPE) were run to evaluate catalysis and to identify the product(s). The head space of the cell after CPE at -2.21 V was analyzed by GC, and CO was observed as the only product after CPE with 92(5)% Faraday efficiency (FE). However, the current decreases over the course of the experiment when a large overpotential was applied (Figure S5). This indicates catalyst degradation during catalysis at more negative potentials. The maximum TON of 4.1(3) was achieved after applying a potential of -2.21 V for 2 hours.

The production of CO implies the existence of a Fe-CO intermediate, so the direct synthesis of potential Fe-CO species was carried out. Two complexes, [LFe(CO)₂](OTf)₂ (**1-(CO)₂**) and [LFe(CH₃CN)(CO)](OTf)₂ (**1-CO**), were prepared from the reaction of **1** with CO gas (Figure 2). Under a CO atmosphere, **1-(CO)₂** can be obtained. The complex was isolated and fully characterized by the usual methods, including NMR and IR spectroscopies (see experimental details below and Figures S6-S17 in the SI for further details on **1-(CO)** and **1-(CO)₂**). However, when the atmosphere is replaced by N₂, one CO molecule is displaced, leaving **1-CO** with an axial acetonitrile ligand as 6th ligand. The conversion from **1-(CO)₂** ($\tilde{\nu}_{\text{CO}} = 1982 \text{ cm}^{-1}$) to **1-CO** ($\tilde{\nu}_{\text{CO}} = 1938 \text{ cm}^{-1}$) can easily be monitored using IR spectroscopy (Figure S14). Molecular structures of **1-(CO)₂** and **1-CO** determined by X-ray diffraction (Figure 2) allow for a comparison of metric parameters. As expected for the increased π -backbonding to the single CO ligand in **1-CO**, the Fe-CO bond of **1-CO** (1.72 Å) is shorter than either of those in **1-(CO)₂** (1.79 and 1.81 Å). The binding of either one or two CO molecules causes minimal changes to the Fe-C^{NHC} bonds relative to **1**. These observations agree with the ⁵⁷Fe isomer shift and quadrupole splitting parameters observed in zero-field Mößbauer spectroscopy. The shorter Fe-CO bonds, which lead to a compressed 4s orbital and a higher 4s electron density at the iron nucleus, and their increased π -backbonding abilities, which causes less shielding of the 4s orbital, combine for a much lower isomer shift δ for both complexes relative to **1**. The decrease of the quadrupole splitting ΔE_Q upon going from **1** to **1-(CO)₂** reflects an increasingly spherical electron distribution around the nucleus upon the addition of a second CO molecule.

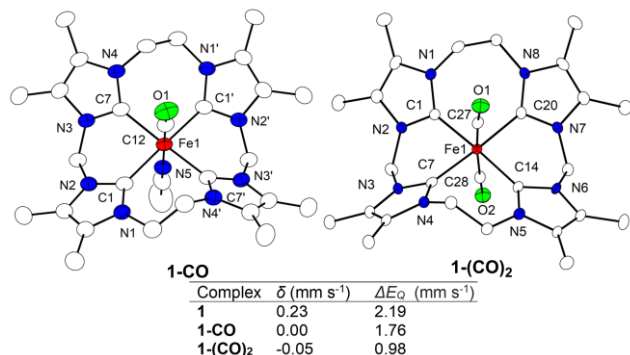


Figure 2. Molecular structures of **1-CO** and **1-(CO)₂** along with ⁵⁷Fe Mößbauer parameters determined at 80 K. Mößbauer data for **1** is from reference ⁵¹.

Since a large excess of CO is necessary to maintain the coordination of both CO molecules in MeCN, subsequent CV studies focused on **1-CO**. The CV data of **1-CO** under a N₂ atmosphere show two reduction peaks with $E_{\text{pc},1} = -2.02 \text{ V}$ and $E_{\text{pc},2} = -2.36 \text{ V}$, $\nu = 0.1 \text{ V s}^{-1}$ (Figure 2, inset). Initial reduction of **1-CO** is irreversible, which suggests that the reduction is accompanied by loss of one axial ligand, as expected for the population of the d_{z²} orbital. The second reduction process shows an anodic feature in the reverse scan at $E_{\text{pa}} = -2.29 \text{ V}$, which gets more prominent with increasing scan rates (Figure S18). Since the potential and reversibility of the second reduction process is distinctly different from the one in **1**, we assume that initial reduction is accompanied by MeCN loss (and not CO loss), as otherwise the same species are formed. In the anodic scan, a further oxidation event occurs at a peak potential $E_{\text{pa}} = -1.49 \text{ V}$, $\nu = 0.1 \text{ V s}^{-1}$. Under a CO₂ atmosphere, there is an appearance of a large reductive wave quite similar to that observed for **1** (Figure 3). The onset of the wave appears after initial reduction of **1-CO**. The half peak potential of the catalytic wave, $E_{\text{cat}/2} = -2.38 \text{ V}$, appears at a nearly identical potential as for **1** and the second reduction event of **1-CO**. The limiting catalytic current and the shape of the catalytic wave is scan rate independent as expected for a catalytic event under purely kinetic conditions (Figure S19).^{56, 57} Headspace analysis after CPE experiments at an applied potential of -2.21 V for 2 hours confirmed CO formation with a FE of 120(13)% and a TON of 7.0(7). The FE of over 100% can be explained by the loss of the axial CO ligand, in this case, likely due to gradual catalyst degradation over the long course of electrocatalysis. As the current drop during catalysis is lower and the TON higher than in the same experiment employing **1**, the stability of **1-CO** under reductive conditions towards catalyst decomposition seems to be higher than that of **1** (Figure S21).

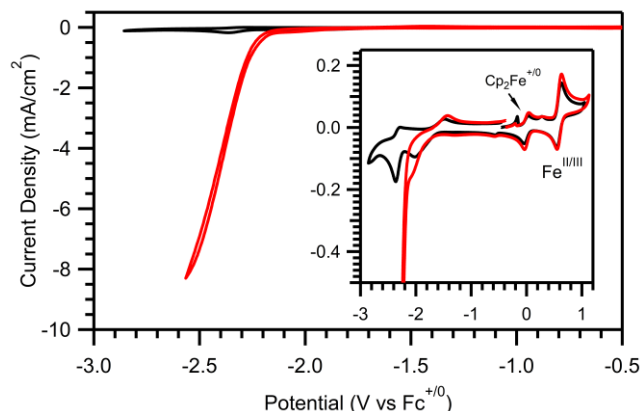


Figure 3. CV of 0.5 mM **1-CO** under a N₂ (black) or CO₂ (red) atmosphere in MeCN + 0.1 M Bu₄NPF₆ scanning towards cathodic potentials at 0.1 V s⁻¹ with glassy carbon disk working electrode. Inset shows reduction under N₂ atmosphere (black) as well as pre-wave of CO₂ reduction wave (red).

In order to compare the efficiency of **1-CO** and **1** under catalytic conditions, the observed rate constants k_{obs} were estimated. The k_{obs} was derived from the limiting catalytic current as the catalytic wave exhibits a pre-wave at the foot of the wave and thus the foot-of-the-wave (FOWA) analysis is

not applicable.^{56, 57} Scan rate dependent CV data of **1** show that catalysis with 1 mM is not under pure kinetic conditions as the data deviate slightly from perfect S-shape and the current depends on the scan rate indicating side phenomena such as substrate consumption (Figure S4).^{56, 57} Thus, the catalyst concentration was decreased to reach kinetic conditions. Indeed, at 0.5 mM, the catalytic current becomes scan rate independent (Figure S22), so that k_{obs} can be estimated according to eq. 1⁵⁸:

$$i_{\text{cat}} = n_{\text{cat}} \cdot F \cdot A \cdot C_{\text{cat}} \cdot \sqrt{D_{\text{cat}} \cdot k_{\text{obs}}} \quad (1)$$

$$k_{\text{obs}} = k_{\text{cat}} [\text{CO}_2]^y \quad (2)$$

Dividing i_{cat} by i_p (current of a reversible non-catalytic event under identical conditions)⁵⁹ eliminates several constants and a plot of i_{cat} over i_p versus $v^{1/2}$ leads to k_{obs} (Figures S22-23)

$$\frac{i_{\text{cat}}}{i_p} = 2.242 \cdot n_{\text{cat}} \sqrt{\frac{R \cdot T}{n_p^3 \cdot F}} \sqrt{k_{\text{obs}}} \sqrt{\frac{1}{v}} \quad (3)$$

n = number of transferred electrons, F = Faraday constant, R = gas constant, v = scan rate; T = temperature, k_{obs} = observed catalytic rate constant.

Since CO must be formed in a disproportionation reaction of two equivalents of the formal CO_2^- radical, the number of transferred electrons equals 2 per CO. This leads to very high k_{obs} values of $7.8 \cdot 10^3 \text{ s}^{-1}$ for **1** and $3.1 \cdot 10^3 \text{ s}^{-1}$ for **1-CO**, among the highest reported catalytic rate constants for a first-row transition metal CO_2 reduction catalyst in the absence of a proton source.

To shed light on the mechanism of CO_2 reduction by both **1** and **1-CO**, linear sweep voltammogram (LSV) spectroelectro-IR (SEC-IR) studies were performed on each complex both under an inert and CO_2 environment in order to monitor putative Fe-CO intermediates. The observed IR spectrum of **1-CO** (Figure 4, top, black) shows a main band at 1938 cm^{-1} , and a small feature at 1981 cm^{-1} originating from minor amounts of **1-(CO)₂**. At the onset of the first reduction process (Figure 4, green), there is an appearance of a CO band at a frequency of 1819 cm^{-1} under N_2 . The shift of the CO band by about -118 cm^{-1} with regard to **1-CO** is characteristic for a metal based reduction forming $[\text{LFe}^{\text{I}}(\text{CO})]^+$ (DFT calculations predict a shift of -95 cm^{-1} upon going from **1-CO** to $[\text{LFe}^{\text{I}}(\text{CO})]^+$; see SI). This supports the hypothesis that initial, irreversible reduction of **1-CO** is accompanied by MeCN loss and not by CO loss. The second reduction is accompanied by the growth of a feature at $\tilde{\nu}_{\text{CO}} = 1730 \text{ cm}^{-1}$ along with the decrease of the putative $[\text{LFe}^{\text{I}}(\text{CO})]^+$ band. The feature at 1730 cm^{-1} is assigned as a $[\text{LFe}^0(\text{CO})]$ species, which however is quite unstable. As soon as it is formed, it vanishes and is replaced by a species with a feature at 1874 cm^{-1} . This is in line with the CV measurements of **1-CO**, where we observed reversibility for the second reduction process at faster scan rates, but not at slower. The instability of the doubly reduced species of **1-CO** was confirmed by chemical reduction. Adding two equivalents of sodium naphthalenide to **1-CO** leads to the formation of a doubly reduced Fe-CO species with the same characteristic CO frequency at 1725 cm^{-1} in the solid state (Figure S30). However, dissolution of this species in MeCN converts it within minutes to two new species, one having the characteristic CO band at a frequency of 1874 cm^{-1} , and

the other being the putative $[\text{LFe}^{\text{I}}(\text{CO})]^+$ intermediate with a band at 1821 cm^{-1} . At very negative potentials there is also an appearance of a feature at 2117 cm^{-1} , similar to that observed in the reduction of acetonitrile under N_2 as seen in Figure S24, which indicates that this band belongs to solvent reduction and is not associated with the complex. Nearly the same species distribution is observed in SEC-IR after initial reduction of **1-(CO)₂** (Figure S27). That is, initial reduction of **1-(CO)₂** leads to the formation of $[\text{LFe}^{\text{I}}(\text{CO})]^+$ ($\nu(\text{CO}) = 1819 \text{ cm}^{-1}$), which indicates that **1-(CO)₂** loses one CO ligand upon reduction. Further reduction forms the species assigned to $[\text{LFe}^0(\text{CO})]$ with a characteristic CO band at a frequency of 1730 cm^{-1} , which then reacts further to form the species with a CO stretching vibration at a frequency of 1874 cm^{-1} .

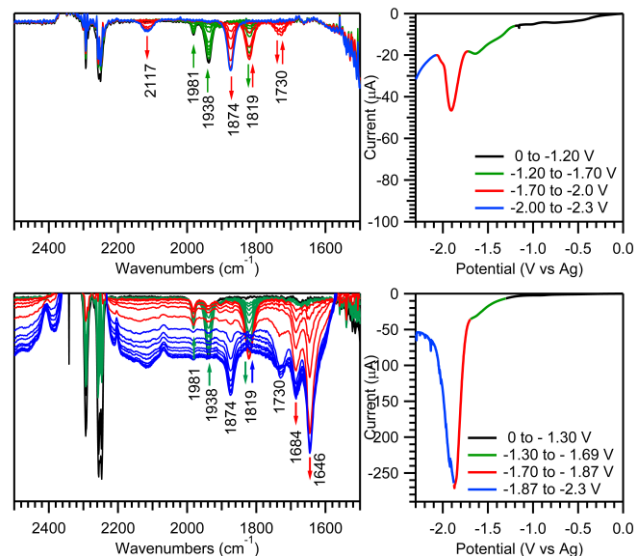


Figure 4. IR changes during the LSV scan of **1-CO** from 0 to -2.3 V (versus Ag wire) in CH_3CN under N_2 (top) or CO_2 (bottom).

Subsequently, SEC-IR of **1-CO** under CO_2 was investigated (Figure 4, bottom). During reduction at the foot of the wave prior catalysis (Figure 4, green), the CO bands of the starting materials at $\tilde{\nu}_{\text{CO}} = 1938 \text{ cm}^{-1}$ (major, **1-CO**) and $\tilde{\nu}_{\text{CO}} = 1981 \text{ cm}^{-1}$ (minor **1-(CO)₂**) decrease, and that assigned to the putative $[\text{LFe}^{\text{I}}\text{-CO}]^+$ species increases ($\tilde{\nu}_{\text{CO}} = 1819 \text{ cm}^{-1}$). At the onset of the catalytic wave (Figure 4, red), bands at frequencies of 1685 and 1645 cm^{-1} appear which are characteristic for HCO_3^- and CO_3^{2-} .²⁹ Under catalytic conditions no Fe^0 species is observed by SEC-IR and $[\text{LFe}^{\text{I}}(\text{CO})]^+$ represents the steady state species. When the potential is scanned beyond the catalytic wave, the current decreases indicating that CO_2 is consumed, the baseline of the IR spectra shifts, reflecting the evolution of CO gas, (Figure 4, blue). Furthermore, the characteristic CO band of $[\text{LFe}^{\text{I}}(\text{CO})]^+$ disappears and is replaced by the CO signature band of $[\text{LFe}^0(\text{CO})]$ at 1730 cm^{-1} . This species decomposes quickly as observed in the absence of CO_2 forming the species with a CO frequency at 1874 cm^{-1} . The band at 1874 cm^{-1} appears after current drop, that is after catalysis, and thus, it does not likely represent a species that is relevant to the catalytic cycle.

SEC-IR of **1** under N_2 (Figure S25) does not show any characteristic features, as expected considering the absence of a

potential Fe-CO motif. However, bands characteristic for Fe-CO species occur during catalysis under a CO₂ atmosphere (Figure 5), most of which have been observed also with **1-CO**. Upon reduction of **1** under catalytic conditions, several species occur nearly simultaneously, namely [LFe^I(CO)]⁺ ($\tilde{\nu}_{\text{CO}}$ = 1819 cm⁻¹), **1-(CO)₂** (1981 cm⁻¹), the decomposition product of [LFe⁰(CO)] ($\tilde{\nu}_{\text{CO}}$ = 1874 cm⁻¹), a previously unobserved species with a CO band at $\tilde{\nu}_{\text{CO}}$ = 1902 cm⁻¹, and slightly later also **1-CO** ($\tilde{\nu}_{\text{CO}}$ = 1938 cm⁻¹), Figure 5. Since only the bands corresponding to HCO₃⁻ and CO₃²⁻ can be seen in the blank reduction of CO₂ in MeCN at very negative potentials, all of the other bands are resulting from the reduction of the iron complex.⁶⁰

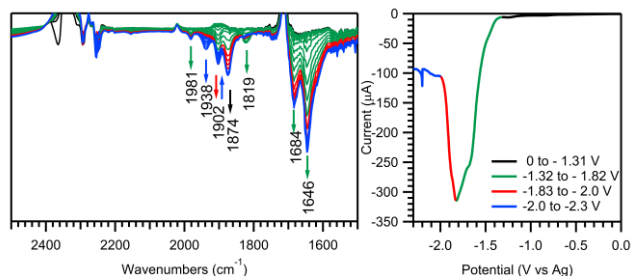
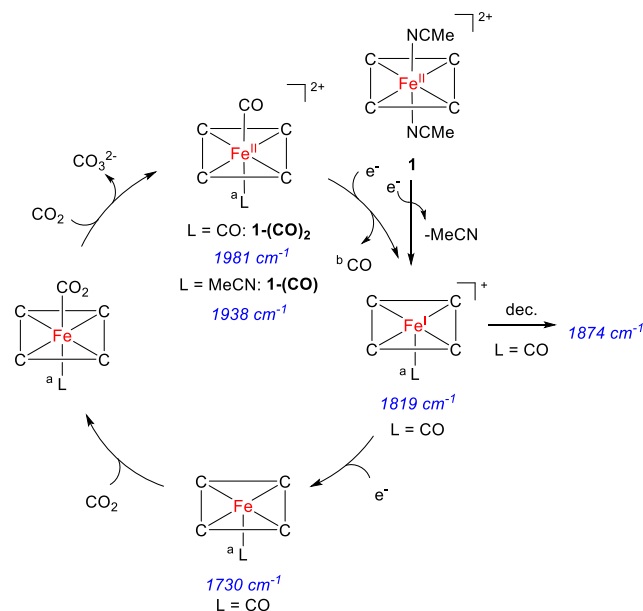


Figure 5. IR changes during the LSV scan of **1** from 0 to -2.3 V in MeCN under CO₂.

The appearance of Fe-CO bands during the electrocatalytic reduction of CO₂ by **1** implies the formation of **1-CO** and its reduced products after initial catalytic turnover. However, there is less formation of [LFe^I(CO)]⁺ (1819 cm⁻¹) relative to that observed in the electrocatalysis by **1-CO** and a more significant growth of the species with a CO band at a frequency of 1874 cm⁻¹. The greater formation of putative decay species and diminished formation of the [LFe^I(CO)]⁺ species proposed to be important to the catalytic cycle likely explains why **1** is less able to sustain catalysis than **1-CO**.

Taking all measurements together, some general mechanistic considerations can be developed. The formation of CO in the absence of protons necessitates a disproportionation reaction of two formal CO₂⁻ radical species to produce CO and CO₃²⁻.⁶¹ Evidence for the production of CO₃²⁻ is obtained in the SEC-IR experiments. This was also the proposed mechanism for the purely organometallic manganese catalyst **IV** (Scheme 1) described above²⁹ and for (2',2'-bipyridine)Re(CO)₃Cl, which also catalyzes the CO₂-to-CO/CO₃²⁻ conversion. In the latter case, a dimeric rhenium species was postulated as crucial intermediate.⁶² Thus, we determined the reaction order in **1**. Concentration dependent measurements of the limiting current i_{cat} revealed a linear dependency on $c(\mathbf{1})$, which indicates that catalysis is first order in **1** and thus no dimeric species is formed in the rate determining step (Figure S31). Since we observe a very high current increase even in the presence of only 0.5 mM of **1** and **1-CO**, the formation of a dimeric species or a homogeneous electron transfer between two reduced species in a non-rate determining step seems unlikely and thus, we assume that CO and CO₃²⁻ are formed by the reaction of a reduced Fe-CO₂ intermediate with a second equivalent of CO₂, which is present in large excess (*cf.* 0.26 M in acetonitrile).⁶³

Initial reduction of **1** and of **1-CO** under catalytic condition appears at the same potential as under N₂, and thus, a pre-equilibrium between **1** or **1-CO** and CO₂ is unlikely. Reduction of **1** is likely accompanied by loss of MeCN to give [LFe^I(NCMe)]⁺ in a fast pre-equilibrium as its reduction appears quasi-reversible in the CV (*vide supra*). Initial reduction of **1-CO** is irreversible and appears at more negative potentials than of **1** and thus, we assume that initial reduction of **1-CO** is accompanied by MeCN loss forming the pentacoordinated [LFe^I(CO)]⁺ species, which is in accordance with the IR-SEC results. The loss of MeCN as a ligand is supported by DFT calculations, where the most stable Fe^I (d⁷) species derived from either **1** or **1-CO** showed the loss of an axial MeCN ligand after optimization (Tables S3-S4). The same [LFe^I(CO)]⁺ species is also formed upon reduction of **1-(CO)₂** via CO loss. DFT calculations furthermore confirm that reduction is metal-centered, the SOMO of [LFe^I(CO)]⁺ and [LFe^I(NCMe)]⁺ having largely d_{z²} character and being polarized towards the open axial site (see Figures S47 and S49). The half-peak potentials of the catalytic waves are almost at the same potentials as the second reduction of **1-CO** indicating that CO₂ binds at the highly nucleophilic metal center in the Fe⁰ (d⁸) state. This is in line with IR-SEC experiments where [LFe^I(CO)]⁺ was identified as steady state species under catalytic conditions. Since **1-(CO)₂** is observed as minor species in IR-SEC under catalytic conditions with **1** and **1-CO**, we tentatively assume that the reaction of the doubly reduced species with a second equivalent of CO₂ is followed by formation of CO₃²⁻ and **1-(CO)₂**. Finally, **1-(CO)₂** is then reduced, which closes the catalytic cycle to re-form the pentacoordinated [LFe^I(CO)]⁺ species (Scheme 2). After initial turnover with **1**, the same species are present as with **1-CO**. However, the reduced species seems to be less stable in the former case as two side products are rapidly detected in the SEC-IR experiment of **1** and CO₂ during catalysis with one being the decomposition product of the doubly reduced **1-CO** species, whereas in the experiment employing **1-CO** this species was only observed after catalysis.



Scheme 2. Proposed mechanism of electrocatalytic CO₂ reduction catalyzed by **1** and **1-CO**. After the first turnover, **1** should follow the same mechanism as **1-CO**. Notes: ^a L = CO except for the first turnover with **1**, there L = MeCN; ^b MeCN is released rather than CO in the first turnover with **1**.

SUMMARY AND CONCLUSIONS

The tetracarbene-iron complexes **1** and **1-CO** catalyze the selective electroreduction of CO₂ to CO and CO₃²⁻ through a disproportionation mechanism in the absence of a proton source. **1** displays a very fast rate of catalytic turnover ($k_{\text{obs}} = 7.8 \cdot 10^3 \text{ s}^{-1}$), but only modest turnover numbers in bulk experiments (TON = 4) because it degrades rather quickly under catalytic conditions. When CO is bound in one of the axial coordination sites as in **1-CO**, the stability is significantly increased (TON = 7.6) while the rate of catalysis decreases only slightly ($k_{\text{obs}} = 3.1 \cdot 10^3 \text{ s}^{-1}$). **1** and **1-CO** represent the first examples of NHC-ligated iron complexes that are capable of electrocatalytically reducing CO₂ to CO.

Iron porphyrin complexes are among the most efficient and well-studied molecular electrocatalysts for the reduction of CO₂ to CO.⁴⁶ The present work now introduces macrocyclic tetracarbene iron complexes such as **1**, which can be viewed as organometallic heme analogues, as a new catalyst class in the field. While macrocyclic tetracarbenes are topologically reminiscent of porphyrins and provide a strong equatorial ligand scaffold alike, they are electronically distinct. In particular, for low-valent tetracarbene iron species responsible for CO₂ reduction, the electronic configuration is expected to be a cobalamin-like “supernucleophile” with electrons occupying the d_{z²} orbital rather than the d_{x²-y²} or ligand-based orbitals.⁴⁰ Indeed, the rather large catalytic reaction rate supports this beneficial electronic structure effect.

The synthetic versatility of the tetracarbene macrocycle is an additional benefit of the new catalyst class, as it offers a wide range of tunability including modifications of both the macrocycle ring size and charge as well as the imidazole back-bone substituents.^{35, 38, 39, 45, 51, 52} As demonstrated, the sixth coordination site at the iron ion, *trans* to the CO₂ binding site, can be used to modulate the catalytic activity and to increase the stability of the complex under reductive conditions. This work paves the way towards establishing NHC-based organometallic heme analogues as efficient and tunable CO reduction electrocatalysts, complementing the archetypical Fe-porphyrin systems.

EXPERIMENTAL DETAILS

Materials and Instrumentation. Solvents were obtained in reagent grade or better and then dried and degassed according to standard procedures before use. Air-sensitive experiment were carried out in a dry nitrogen atmosphere primarily in an MBraun LabMaster glovebox or using standard Schlenk techniques. NMR spectra were recorded on a Bruker Avance III HD 500 and a Bruker Avance III 300 spectrometer at a temperature of 298 K if not stated otherwise. Chemical shifts are reported in parts per million in relation to tetramethylsilane and referenced to the residual hydrogen atoms of the used deuterated solvents or their natural abundance ¹³C resonances.⁶⁴ ⁵⁷Fe Mößbauer spectra were

measured using a ⁵⁷Co source in a Rh matrix using an alternating constant acceleration Wissel Mößbauer spectrometer equipped with a Janis closed-cycle helium cryostat. Transmission data were collected, and isomer shifts are reported relative to iron metal at ambient temperature. Experimental data were simulated with *Mfit software*.⁶⁵

Cyclic voltammograms and electrocatalysis experiments were recorded on a NOVA/Autolab potentiostat in a home-made gas-tight cell with a glassy carbon working electrode, platinum wire counter electrode, and silver wire *pseudo*-reference electrode. The CV spectra were referenced to the Fc^{0/+} couple that was recorded under exact experimental conditions as an external reference in the cases where ferrocene or decamethylferrocene were not explicitly used as an internal reference. All electrochemical measurements were performed in a dry and degassed acetonitrile solution with 0.1 M tetrabutylammonium hexafluorophosphate under a N₂ or a CO₂ environment. Ohmic drop was carefully compensated during CV measurements using NOVA 2.1.2 software. The same air-tight cell and electrode configuration was used for electrocatalysis experiments; however, the Pt wire counter electrode was separated from the bulk solution by a fritted-glass bridge. Solutions were prepared in a glovebox and sealed in an air-tight cell and studied either under N₂ or by purging the cell with CO₂ for a minimum of 10 minutes (concentration of CO₂ in saturated CH₃CN solution = 0.26 M).⁶³ For GC measurements of gaseous products of CO₂ reduction, 0.5 ml CH₄ was added to the electrochemical cell for use as an internal standard in the GC. After electrolysis, gaseous products were measured and quantified with a Shimadzu GC-2014 equipped with a thermal conductivity detector (TDC) and a ShinCarbon ST 80/100 silico column with either argon carrier gas (detection of H₂) or helium carrier gas (detection of CO). Calibration curves were made by injecting varied known quantities of CO into the electrochemical cell with a fixed amount of CH₄ and measuring the peak areas.

Synthesis and Characterization. [H₄L](OTf)₄ and [LFe(CH₃CN)₂](OTf)₂ (**1**) were synthesized according to previously reported methods without modification.⁵¹

[LFe^{II}(CO)₂](OTf)₂ (**1-(CO)₂**) was synthesized by freeze-pump-thawing a solution of **1** in MeCN (10 mL) and charging the flask with CO gas. After stirring the resulting solution at room temperature for 2 d, Et₂O was added until a precipitate formed. The colorless solid was recrystallized from DCM/Et₂O and dried under reduced pressure. Single crystals suitable for X-ray diffraction analysis were gathered from slow diffusion of Et₂O into a DCM solution of the product. [LFe^{II}(CO)₂](OTf)₂ was further characterized by ¹H NMR, ¹³C NMR, IR, and DFT:IR spectroscopies. When the CO atmosphere is removed, the resulting complex is a mixture of **1-(CO)₂** and **1-CO**, and the transition from one to the other can be observed in both NMR and IR (Figure S14). ¹H NMR (300 MHz, CD₃CN): δ = 5.85 (s, 4H, NCH₂N), 4.49 (s, 8H, NCH₂CH₂N), 2.30 (d, *J* = 0.8 Hz, 12H, CH₃), 2.21 (d, *J* = 0.8 Hz, 12H, CH₃) ppm. ¹³C{¹H} NMR (75 MHz, CD₃CN): δ = 212.1 (CO), 172.6 (C^{2-Im}), 130.1 (C^{Im}), 128.3 (C^{Im}), 122.2 (q, *J*(¹³C-¹⁹F) = 321 Hz, SO₃CF₃), 56.9 (NCH₂N), 46.5 (NCH₂CH₂N), 9.7 (C^{ImMe}), 9.3 (C^{ImMe}) ppm. IR (ATR, CH₃CN): $\tilde{\nu}$ = 2995 (w), 2942 (w), **1982 (s)**, 1674 (w), 1663 (w), 1484 (w), 1463

(w), 1448 (w), 1413 (w), 1398 (w), 1385 (w), 1366 (w), 1333 (w), 1271 (s), 1225 (m), 1156 (s), 1033 (s), 997 (w), 893 (w), 865 (w), 755 (w), 714 (w), 695 (w) cm^{-1} . MS (ESI⁺ CH₃CN): m/z = 693.1 ([LFe^{II}(CO)(OTf)]⁺) CO likely lost during ionization. CV (1.1 mM, (0.1M TBAPF₆) CH₃CN) – oxidation potential at 0.96 V (vs. Fc^{+/0}, 0.1 V s⁻¹). Mößbauer (80 K): δ = -0.04 mm s⁻¹, ΔE_Q = 0.97 mm s⁻¹.

[LFe^{II}(CO)(MeCN)](OTf)₂ (**1-CO**) was synthesized by dissolving 25 mg of **1** (2.8×10^{-5} mol) in 1.5 mL CH₃CN and sealed in a Schlenk tube in a glovebox. The Schlenk tube was removed from the glovebox and connected to a Schlenk line connected to CO gas. The solution was frozen and the N₂ atmosphere was removed by vacuum. The flask was then charged with 1 bar CO gas and allowed to thaw. This reaction mixture was stirred overnight before removing the excess CO through several freeze-pump-thaw cycles. The sealed Schlenk tube was taken back into a glovebox where repeated recrystallizations of slow diffusion of Et₂O into very concentrated CH₃CN solutions of **1-CO** allowed for the isolation of dark yellow boxy crystals suitable for characterization by single crystal X-ray diffraction. However, there were also very thin red-brown needles present in the solid that could not be separated. The solid was otherwise pure by Mößbauer and cyclic voltammetry, so the impurity is likely insignificant. [LFe^{II}(CO)(MeCN)](OTf)₂ was further characterized by ¹H NMR, ¹³C NMR, IR, DFT:IR, and ESI-MS. [LFe^{II}(CO)(MeCN)](OTf)₂ can also be prepared by removing the CO atmosphere of [LFe^{II}(CO)₂](OTf)₂, the conversion was monitored by IR. ¹H NMR (300 MHz, CD₃CN): δ = 5.92 (d, J = 14.2 Hz, 2H, NCH₂N), 5.73 (d, J = 13.9 Hz, 2H, NCH₂N), 4.70 (dd, J = 14.4, 7.6 Hz, 4H, NCH₂CH₂N), 4.32 (dd, J = 14.0, 6.6 Hz, 4H, NCH₂CH₂N), 2.32 (d, J = 0.8 Hz, 12H, CH₃), 2.22 (d, J = 0.7 Hz, 12H, CH₃) ppm. ¹³C{¹H} NMR (125 MHz, CD₃CN): δ = 224.1 (CO), 181.7 (C^{2-im}), 128.6 (C^{im}), 127.4 (C^{im}), 122.1 (q, $J(^{13}\text{C}-^{19}\text{F})$ = 321 Hz, SO₃CF₃), 56.8 (NCH₂N), 46.4 (NCH₂CH₂N), 9.6 (C^{imMe}), 9.3 (C^{imMe}) ppm. IR (ATR, CH₃CN): $\tilde{\nu}$ = 2996 (w), 2942 (w), **1938** (s), 1680 (w), 1661 (w), 1475 (w), 1445 (w), 1409 (w), 1376 (m), 1331 (w), 1271 (s), 1225 (s), 1156 (m), 1033 (s), 915 (w), 891 (w), 744 (w), 714 (w) cm^{-1} . MS (ESI⁺ CH₃CN): m/z = 693.1 ([LFe^{II}(CO)(OTf)]⁺). CV (1 mM, (0.1M TBAPF₆) CH₃CN) – oxidation potential at 0.61 V (vs. Fc^{+/0}, 0.1 V s⁻¹). Mößbauer (80 K): δ = 0.00 mm s⁻¹, ΔE_Q = 1.76 mm s⁻¹.

X-Ray Crystallography. Crystal data and details of the data collections are given in Table S1, selected bond lengths angles in Table S2, molecular structures are shown in Figures S32-33. X-ray data for [LFe(CO)₂](OTf)₂ (**1-(CO)₂**) were collected on a STOE IPDS II diffractometer (graphite monochromated Mo-K α radiation, λ = 0.71073 Å) by use of ω scans at RT or -140 °C. X-ray data for [LFe(CO)(MeCN)](OTf)₂ (**1-(CO)**) were collected at room temperature under otherwise same conditions, since decomposition of the crystals at lower temperatures has been observed. The structures were solved with SHELXT and refined on F^2 using all reflections with SHELXL-2018.^{66,67} Non-hydrogen atoms were refined anisotropically. Hydrogen atoms were placed in calculated positions and assigned to an isotropic displacement parameter of 1.5/1.2 $U_{\text{eq}}(\text{C})$.

The CF₃SO₃⁻ counterion in [LFe(CO)(MeCN)](OTf)₂ was found to be disordered (occupancy factors: 0.879(4) /

0.121(4)). SAME and RIGU restraints and EADP constraints were used to model the disordered counterion. The unit cell of [LFe(CO)₂](OTf)₂ contains highly disordered solvent molecules (dichloromethane and diethyl ether) for which no satisfactory model for a disorder could be found. The solvent contribution to the structure factors was calculated with PLATON SQUEEZE⁶⁸ and the resulting .fab file was processed with SHELXL using the ABIN instruction. The empirical formula and derived values are in accordance with the calculated cell content. Face-indexed absorption corrections were performed numerically with the program X-RED.⁶⁹

DFT calculations. The ORCA program package (version 4.2.1) was employed for all calculations.⁷⁰ Geometry optimization and frequency calculation was performed starting from the crystallographic data (BP86 functional, def2-tzvp basis set,^{71,72} RI approximation using the auxiliary def2/J basis set, D3 dispersion correction with Becke-Johnson damping,⁷³ tight convergence and optimization criteria). Additional details regarding calculations as well as structures, tables of relevant bond lengths, and calculated IR spectra can be found in the supporting information.

ASSOCIATED CONTENT

A supporting information document that includes additional figures, spectroscopic characterization, crystallographic information and DFT calculated structures and IR spectra is available free of charge via the Internet at <http://pubs.acs.org>.

AUTHOR INFORMATION

Corresponding Authors

Inke Siewert, Institute of Inorganic Chemistry and International Center for Advanced Studies of Energy Conversion (ICASEC) and Wöhler Research Institute for Sustainable Chemistry (WISCh), University of Göttingen, D-37077 Göttingen, Germany; orcid.org/0000-0003-3121-3917; Email: inke.siewert@chemie.unigoettingen.de

Franc Meyer, Institute of Inorganic Chemistry and International Center for Advanced Studies of Energy Conversion (ICASEC) and Wöhler Research Institute for Sustainable Chemistry (WISCh), University of Göttingen, D-37077 Göttingen, Germany; orcid.org/0000-0002-8613-7862 ; Email: franc.meyer@chemie.unigoettingen.de

Author Contributions

The manuscript was written through contributions of all authors. All authors have given approval to the final version of the manuscript.

Funding Sources

This project has been supported by the University of Göttingen and partly funded by the Deutsche Forschungsgemeinschaft (DFG, German Research Foundation) via 217133147/SFB 1073, project C01.

Notes

The authors declare no conflicts of interest.

ACKNOWLEDGMENTS

The authors are grateful to Maike Niepel, Lucas A. Paul, Alexander Wilting, and Igor Fokin (all University of Göttingen) for their assistance during GC measurements and IR-SEC experiments.

REFERENCES

- Lewis, N. S.; Nocera, D. G., Powering the planet: Chemical challenges in solar energy utilization. *Proc. Natl. Acad. Sci. U.S.A.* **2006**, *103* (43), 15729-15735.
- Lense, S.; Grice, K. A.; Gillette, K.; Wolf, L. M.; Robertson, G.; McKeon, D.; Saucedo, C.; Carroll, P. J.; Gau, M., Effects of Tuning Intramolecular Proton Acidity on CO₂ Reduction by Mn Bipyridyl Species. *Organometallics* **2020**, *39* (13), 2425-2437.
- Qiao, J.; Liu, Y.; Hong, F.; Zhang, J., A review of catalysts for the electroreduction of carbon dioxide to produce low-carbon fuels. *Chem. Soc. Rev.* **2014**, *43* (2), 631-675.
- Costentin, C.; Passard, G.; Robert, M.; Savéant, J.-M., Pendant Acid-Base Groups in Molecular Catalysts: H-Bond Promoters or Proton Relays? Mechanisms of the Conversion of CO₂ to CO by Electrogenated Iron(0)Porphyrins Bearing Prepositioned Phenol Functionalities. *J. Am. Chem. Soc.* **2014**, *136* (33), 11821-11829.
- Costentin, C.; Drouet, S.; Robert, M.; Savéant, J.-M., A Local Proton Source Enhances CO₂ Electroreduction to CO by a Molecular Fe Catalyst. *Science* **2012**, *338* (6103), 90-94.
- Azcarate, I.; Costentin, C.; Robert, M.; Savéant, J.-M., Through-Space Charge Interaction Substituent Effects in Molecular Catalysis Leading to the Design of the Most Efficient Catalyst of CO₂-to-CO Electrochemical Conversion. *J. Am. Chem. Soc.* **2016**, *138* (51), 16639-16644.
- Torbensen, K.; Han, C.; Boudy, B.; von Wolff, N.; Bertail, C.; Braun, W.; Robert, M., Iron Porphyrin Allows Fast and Selective Electrocatalytic Conversion of CO₂ to CO in a Flow Cell. *Chem. Eur. J.* **2020**, *26* (14), 3034-3038.
- Sinha, S.; Warren, J. J., Unexpected Solvent Effect in Electrocatalytic CO₂ to CO Conversion Revealed Using Asymmetric Metalloporphyrins. *Inorg. Chem.* **2018**, *57* (20), 12650-12656.
- Azcarate, I.; Costentin, C.; Robert, M.; Savéant, J.-M., Dissection of Electronic Substituent Effects in Multielectron-Multistep Molecular Catalysis. Electrochemical CO₂-to-CO Conversion Catalyzed by Iron Porphyrins. *J. Phys. Chem. C* **2016**, *120* (51), 28951-28960.
- Mondal, B.; Sen, P.; Rana, A.; Saha, D.; Das, P.; Dey, A., Reduction of CO₂ to CO by an Iron Porphyrin Catalyst in the Presence of Oxygen. *ACS Catal.* **2019**, *9* (5), 3895-3899.
- Sen, P.; Mondal, B.; Saha, D.; Rana, A.; Dey, A., Role of 2nd sphere H-bonding residues in tuning the kinetics of CO₂ reduction to CO by iron porphyrin complexes. *Dalton Trans.* **2019**, *48* (18), 5965-5977.
- Gotico, P.; Boitrel, B.; Guillot, R.; Sircoglou, M.; Quaranta, A.; Halime, Z.; Leibl, W.; Aukauloo, A., Second-Sphere Biomimetic Multipoint Hydrogen-Bonding Patterns to Boost CO₂ Reduction of Iron Porphyrins. *Angew. Chem. Int. Ed.* **2019**, *58* (14), 4504-4509.
- Cometto, C.; Chen, L.; Lo, P.-K.; Guo, Z.; Lau, K.-C.; Anxolabéhère-Mallart, E.; Fave, C.; Lau, T.-C.; Robert, M., Highly Selective Molecular Catalysts for the CO₂-to-CO Electrochemical Conversion at Very Low Overpotential. Contrasting Fe vs Co Quaterpyridine Complexes upon Mechanistic Studies. *ACS Catal.* **2018**, *8* (4), 3411-3417.
- Cometto, C.; Chen, L.; Anxolabéhère-Mallart, E.; Fave, C.; Lau, T.-C.; Robert, M., Molecular Electrochemical Catalysis of the CO₂-to-CO Conversion with a Co Complex: A Cyclic Voltammetry Mechanistic Investigation. *Organometallics* **2019**, *38* (6), 1280-1285.
- Bourrez, M.; Molton, F.; Chardon-Noblat, S.; Deronzier, A., [Mn(bipyridyl)(CO)₃Br]: An Abundant Metal Carbonyl Complex as Efficient Electrocatalyst for CO₂ Reduction. *Angew. Chem. Int. Ed.* **2011**, *50* (42), 9903-9906.
- Sampson, M. D.; Nguyen, A. D.; Grice, K. A.; Moore, C. E.; Rheingold, A. L.; Kubiak, C. P., Manganese Catalysts with Bulky Bipyridine Ligands for the Electrocatalytic Reduction of Carbon Dioxide: Eliminating Dimerization and Altering Catalysis. *J. Am. Chem. Soc.* **2014**, *136* (14), 5460-5471.
- Machan, C. W.; Stanton, C. J.; Vandezande, J. E.; Majetich, G. F.; Schaefer, H. F.; Kubiak, C. P.; Agarwal, J., Electrocatalytic Reduction of Carbon Dioxide by Mn(CN)(2,2'-bipyridine)(CO)₃: CN Coordination Alters Mechanism. *Inorg. Chem.* **2015**, *54* (17), 8849-8856.
- Sampson, M. D.; Kubiak, C. P., Manganese Electrocatalysts with Bulky Bipyridine Ligands: Utilizing Lewis Acids To Promote Carbon Dioxide Reduction at Low Overpotentials. *J. Am. Chem. Soc.* **2016**, *138* (4), 1386-1393.
- Ngo, K. T.; McKinnon, M.; Mahanti, B.; Narayanan, R.; Grills, D. C.; Ertem, M. Z.; Rochford, J., Turning on the Protonation-First Pathway for Electrocatalytic CO₂ Reduction by Manganese Bipyridyl Tricarbonyl Complexes. *J. Am. Chem. Soc.* **2017**, *139* (7), 2604-2618.
- Bourrez, M.; Orio, M.; Molton, F.; Vezin, H.; Duboc, C.; Deronzier, A.; Chardon-Noblat, S., Pulsed-EPR Evidence of a Manganese(II) Hydroxycarbonyl Intermediate in the Electrocatalytic Reduction of Carbon Dioxide by a Manganese Bipyridyl Derivative. *Angew. Chem. Int. Ed.* **2014**, *53* (1), 240-243.
- Smieja, J. M.; Sampson, M. D.; Grice, K. A.; Benson, E. E.; Froehlich, J. D.; Kubiak, C. P., Manganese as a Substitute for Rhenium in CO₂ Reduction Catalysts: The Importance of Acids. *Inorg. Chem.* **2013**, *52* (5), 2484-2491.
- Boutin, E.; Merakeb, L.; Ma, B.; Boudy, B.; Wang, M.; Bonin, J.; Anxolabéhère-Mallart, E.; Robert, M., Molecular catalysis of CO₂ reduction: recent advances and perspectives in electrochemical and light-driven processes with selected Fe, Ni and Co aza macrocyclic and polypyridine complexes. *Chem. Soc. Rev.* **2020**, *49* (16), 5772-5809.
- Thoi, V. S.; Chang, C. J., Nickel N-heterocyclic carbene-pyridine complexes that exhibit selectivity for electrocatalytic reduction of carbon dioxide over water. *ChemComm* **2011**, *47* (23), 6578-6580.
- Cope, J. D.; Liyanage, N. P.; Kelley, P. J.; Denny, J. A.; Valente, E. J.; Webster, C. E.; Delcamp, J. H.; Hollis, T. K., Electrocatalytic reduction of CO₂ with CCC-NHC pincer nickel complexes. *ChemComm* **2017**, *53* (68), 9442-9445.
- Ostericher, A. L.; Porter, T. M.; Reineke, M. H.; Kubiak, C. P., Thermodynamic targeting of electrocatalytic CO₂ reduction: advantages, limitations, and insights for catalyst design. *Dalton Trans.* **2019**, *48* (42), 15841-15848.
- Su, X.; McCardle, K. M.; Panetier, J. A.; Jurss, J. W., Electrocatalytic CO₂ reduction with nickel complexes supported by tunable bipyridyl-N-heterocyclic carbene donors: understanding redox-active macrocycles. *ChemComm* **2018**, *54* (27), 3351-3354.
- Shirley, H.; Su, X.; Sanjanwala, H.; Talukdar, K.; Jurss, J. W.; Delcamp, J. H., Durable Solar-Powered Systems with Ni-Catalysts for Conversion of CO₂ or CO to CH₄. *J. Am. Chem. Soc.* **2019**, *141* (16), 6617-6622.
- Su, X.; McCardle, K. M.; Chen, L.; Panetier, J. A.; Jurss, J. W., Robust and Selective Cobalt Catalysts Bearing Redox-Active Bipyridyl-N-heterocyclic Carbene Frameworks for Electrochemical CO₂ Reduction in Aqueous Solutions. *ACS Catal.* **2019**, *9* (8), 7398-7408.
- Franco, F.; Pinto, M. F.; Royo, B.; Lloret-Fillol, J., A Highly Active N-Heterocyclic Carbene Manganese(I) Complex for Selective Electrocatalytic CO₂ Reduction to CO. *Angew. Chem. Int. Ed.* **2018**, *57* (17), 4603-4606.

30. Yang, Y.; Zhang, Z.; Chang, X.; Zhang, Y.-Q.; Liao, R.-Z.; Duan, L., Highly Active Manganese-Based CO₂ Reduction Catalysts with Bulky NHC Ligands: A Mechanistic Study. *Inorg. Chem.* **2020**, *59* (14), 10234-10242.
31. Cordes, C.; Morganti, M.; Klawitter, I.; Schremmer, C.; Dechert, S.; Meyer, F., Disproportionation Equilibrium of a μ -Oxodiiron(III) Complex Giving Rise to C-H Activation Reactivity: Structural Snapshot of a Unique Oxoiron(IV) Adduct. *Angew. Chem. Int. Ed.* **2019**, *58* (32), 10855-10858.
32. Kupper, C.; Mondal, B.; Serrano-Plana, J.; Klawitter, I.; Neese, F.; Costas, M.; Ye, S.; Meyer, F., Nonclassical Single-State Reactivity of an Oxo-Iron(IV) Complex Confined to Triplet Pathways. *J. Am. Chem. Soc.* **2017**, *139* (26), 8939-8949.
33. Dyckhoff, F.; Schlagintweit, J. F.; Reich, R. M.; Kühn, F. E., Pushing the limits of activity and stability: the effects of Lewis acids on non-heme iron-NHC epoxidation catalysts. *Catal. Sci. Technol.* **2020**, *10* (11), 3532-3536.
34. Kück, J. W.; Anneser, M. R.; Hofmann, B.; Pöthig, A.; Cokoja, M.; Kühn, F. E., Fighting Fenton Chemistry: A Highly Active Iron(III) Tetracarbene Complex in Epoxidation Catalysis. *ChemSusChem* **2015**, *8* (23), 4056-4063.
35. Anneser, M. R.; Haslinger, S.; Pöthig, A.; Cokoja, M.; Basset, J.-M.; Kühn, F. E., Synthesis and Characterization of an Iron Complex Bearing a Cyclic Tetra-N-heterocyclic Carbene Ligand: An Artificial Heme Analogue? *Inorg. Chem.* **2015**, *54* (8), 3797-3804.
36. Anneser, M. R.; Haslinger, S.; Pöthig, A.; Cokoja, M.; D'Elia, V.; Högerl, M. P.; Basset, J.-M.; Kühn, F. E., Binding of molecular oxygen by an artificial heme analogue: investigation on the formation of an Fe-tetracarbene superoxo complex. *Dalton Trans.* **2016**, *45* (15), 6449-6455.
37. Isbill, S. B.; Chandrachud, P. P.; Kern, J. L.; Jenkins, D. M.; Roy, S., Elucidation of the Reaction Mechanism of C2 + N1 Aziridination from Tetracarbene Iron Catalysts. *ACS Catal.* **2019**, *9* (7), 6223-6233.
38. Chandrachud, P. P.; Bass, H. M.; Jenkins, D. M., Synthesis of Fully Aliphatic Aziridines with a Macrocyclic Tetracarbene Iron Catalyst. *Organometallics* **2016**, *35* (11), 1652-1657.
39. Cramer, S. A.; Jenkins, D. M., Synthesis of Aziridines from Alkenes and Aryl Azides with a Reusable Macrocyclic Tetracarbene Iron Catalyst. *J. Am. Chem. Soc.* **2011**, *133* (48), 19342-19345.
40. Ye, S.; Kupper, C.; Meyer, S.; Andris, E.; Navrátil, R.; Krahe, O.; Mondal, B.; Atanasov, M.; Bill, E.; Roithová, J.; Meyer, F.; Neese, F., Magnetic Circular Dichroism Evidence for an Unusual Electronic Structure of a Tetracarbene-Oxoiron(IV) Complex. *J. Am. Chem. Soc.* **2016**, *138* (43), 14312-14325.
41. Anneser, M. R.; Elpitiya, G. R.; Townsend, J.; Johnson, E. J.; Powers, X. B.; DeJesus, J. F.; Vogiatzis, K. D.; Jenkins, D. M., Unprecedented Five-Coordinate Iron(IV) Imides Generate Divergent Spin States Based on the Imide R-Groups. *Angew. Chem. Int. Ed.* **2019**, *58* (24), 8115-8118.
42. Kupper, C.; Rees, J. A.; Dechert, S.; DeBeer, S.; Meyer, F., Complete Series of {FeNO}⁸, {FeNO}⁷, and {FeNO}⁶ Complexes Stabilized by a Tetracarbene Macrocyclic. *J. Am. Chem. Soc.* **2016**, *138* (25), 7888-7898.
43. Kupper, C.; Schober, A.; Demeshko, S.; Bergner, M.; Meyer, F., An Exclusively Organometallic {FeNO}⁷ Complex with Tetracarbene Ligation and a Linear FeNO Unit. *Inorg. Chem.* **2015**, *54* (7), 3096-3098.
44. Meyer, S.; Klawitter, I.; Demeshko, S.; Bill, E.; Meyer, F., A Tetracarbene-Oxoiron(IV) Complex. *Angew. Chem. Int. Ed.* **2013**, *52* (3), 901-905.
45. Anneser, M. R.; Elpitiya, G. R.; Powers, X. B.; Jenkins, D. M., Toward a Porphyrin-Style NHC: A 16-Atom Ringed Dianionic Tetra-NHC Macrocyclic and Its Fe(II) and Fe(III) Complexes. *Organometallics* **2019**, *38* (4), 981-987.
46. Costentin, C.; Robert, M.; Savéant, J.-M., Current Issues in Molecular Catalysis Illustrated by Iron Porphyrins as Catalysts of the CO₂-to-CO Electrochemical Conversion. *Acc. Chem. Res.* **2015**, *48* (12), 2996-3006.
47. Mondal, B.; Rana, A.; Sen, P.; Dey, A., Intermediates Involved in the 2e⁻/2H⁺ Reduction of CO₂ to CO by Iron(0) Porphyrin. *J. Am. Chem. Soc.* **2015**, *137* (35), 11214-11217.
48. Römelt, C.; Ye, S.; Bill, E.; Weyhermüller, T.; van Gastel, M.; Neese, F., Electronic Structure and Spin Multiplicity of Iron Tetraphenylporphyrins in Their Reduced States as Determined by a Combination of Resonance Raman Spectroscopy and Quantum Chemistry. *Inorg. Chem.* **2018**, *57* (4), 2141-2148.
49. Römelt, C.; Song, J.; Tarrago, M.; Rees, J. A.; van Gastel, M.; Weyhermüller, T.; DeBeer, S.; Bill, E.; Neese, F.; Ye, S., Electronic Structure of a Formal Iron(0) Porphyrin Complex Relevant to CO₂ Reduction. *Inorg. Chem.* **2017**, *56* (8), 4745-4750.
50. Saravanan, N.; Balamurugan, M.; Devi, K. S. S.; Nam, K. T.; Senthil Kumar, A., Vitamin B12 (Cyanocobalamin Complex) Immobilized Graphene Oxide for Efficient Electrocatalytic Carbon Dioxide Reduction Reaction. *ChemSusChem* **2020**.
51. Schremmer, C.; Cordes, C.; Klawitter, I.; Bergner, M.; Schiewer, C. E.; Dechert, S.; Demeshko, S.; John, M.; Meyer, F., Spin-State Variations of Iron(III) Complexes with Tetracarbene Macrocycles. *Chem. Eur. J.* **2019**, *25* (15), 3918-3929.
52. DeJesus, J. F.; Jenkins, D. M., A Chiral Macrocyclic Tetra-N-Heterocyclic Carbene Yields an "All Carbene" Iron Alkylidene Complex. *Chem. Eur. J.* **2020**, *26* (6), 1429-1435.
53. Bass, H. M.; Cramer, S. A.; McCullough, A. S.; Bernstein, K. J.; Murdock, C. R.; Jenkins, D. M., Employing Dianionic Macrocyclic Tetracarbenes To Synthesize Neutral Divalent Metal Complexes. *Organometallics* **2013**, *32* (7), 2160-2167.
54. Zanello, P.; Connelly, N. G., *Inorganic Electrochemistry: Theory, Practice and Applications*. Royal Society of Chemistry: 2003.
55. Appel, A. M.; Helm, M. L., Determining the Overpotential for a Molecular Electrocatalyst. *ACS Catal.* **2014**, *4* (2), 630-633.
56. Costentin, C.; Drouet, S.; Robert, M.; Savéant, J.-M., Turnover Numbers, Turnover Frequencies, and Overpotential in Molecular Catalysis of Electrochemical Reactions. Cyclic Voltammetry and Preparative-Scale Electrolysis. *J. Am. Chem. Soc.* **2012**, *134* (27), 11235-11242.
57. Rountree, E. S.; McCarthy, B. D.; Eisenhart, T. T.; Dempsey, J. L., Evaluation of Homogeneous Electrocatalysts by Cyclic Voltammetry. *Inorg. Chem.* **2014**, *53* (19), 9983-10002.
58. Saveant, J. M.; Vianello, E., Potential-sweep chronoamperometry: Kinetic currents for first-order chemical reaction parallel to electron-transfer process (catalytic currents). *Electrochim. Acta* **1965**, *10* (9), 905-920.
59. Bard, A. J.; Faulkner, L. R.; John, W.; Sons, *Electrochemical Methods: Fundamentals and Applications*. John Wiley & Sons: Hoboken, 2007.
60. Wilting, A.; Stolper, T.; Mata, R. A.; Siewert, I., Dinuclear Rhenium Complex with a Proton Responsive Ligand as a Redox Catalyst for the Electrochemical CO₂ Reduction. *Inorg. Chem.* **2017**, *56* (7), 4176-4185.
61. Amatore, C.; Saveant, J. M., Mechanism and kinetic characteristics of the electrochemical reduction of carbon dioxide in media of low proton availability. *J. Am. Chem. Soc.* **1981**, *103* (17), 5021-5023.
62. Agarwal, J.; Fujita, E.; Schaefer, H. F.; Muckerman, J. T., Mechanisms for CO Production from CO₂ Using Reduced Rhenium Tricarbonyl Catalysts. *J. Am. Chem. Soc.* **2012**, *134* (11), 5180-5186.
63. Heimann, J. E.; Bernskoetter, W. H.; Hazari, N.; Mayer, James M., Acceleration of CO₂ insertion into metal hydrides: ligand, Lewis acid, and solvent effects on reaction kinetics. *Chem. Sci.* **2018**, *9* (32), 6629-6638.

64. Gottlieb, H. E.; Kotlyar, V.; Nudelman, A., NMR Chemical Shifts of Common Laboratory Solvents as Trace Impurities. *J. Org. Chem.* **1997**, *62* (21), 7512-7515.
65. E. Bill, Mfit, Max-Planck Institute for Chemical Energy Conversion, Mülheim/Ruhr, Germany, 2008.
66. Sheldrick, G., SHELXT - Integrated space-group and crystal-structure determination. *Acta Crystallogr. A* **2015**, *71* (1), 3-8.
67. Sheldrick, G., Crystal structure refinement with SHELXL. *Acta Crystallogr. C* **2015**, *71* (1), 3-8.
68. Spek, A. L., PLATON SQUEEZE: a tool for the calculation of the disordered solvent contribution to the calculated structure factors. *Acta Crystallogr C Struct Chem* **2015**, *71* (Pt 1), 9-18.
69. X-RED; STOE & CIE GmbH, Darmstadt, Germany, 2002.
70. Neese, F., The ORCA program system. *Wiley Interdisciplinary Reviews: Computational Molecular Science* **2012**, *2* (1), 73-78.
71. Schäfer, A.; Horn, H.; Ahlrichs, R., Fully Optimized Contracted Gaussian Basis Sets for Atoms Lithium to Krypton. *J. Chem. Phys.* **1992**, *97* (4), 2571-2577.
72. Weigend, F.; Ahlrichs, R., Balanced basis sets of split valence, triple zeta valence and quadruple zeta valence quality for H to Rn: Design and assessment of accuracy. *Phys. Chem. Chem. Phys.* **2005**, *7* (18), 3297-3305.
73. Grimme, S.; Antony, J.; Ehrlich, S.; Krieg, H., A consistent and accurate ab initio parametrization of density functional dispersion correction (DFT-D) for the 94 elements H-Pu. *J. Chem. Phys.* **2010**, *132* (15), 154104.